Available online at www.sciencedirect.com
ScienceDirect
Journal of Solid State Chemistry 180 (2007) 2816–2823
JOURNAL OF SOLID STATE CHEMISTRY
www.elsevier.com/locate/jssc

Structural and physical properties of the 6H $BaRuO_3$ polymorph synthesized under high pressure

J.G. Zhao, L.X. Yang, Y. Yu, F.Y. Li, R.C. Yu, Z. Fang, L.C. Chen, C.Q. Jin*

Beijing National Lab for Condensed Matter Physics, Institute of Physics, Chinese Academy of Sciences, Beijing 100080, PR China

Received 8 May 2007; received in revised form 16 July 2007; accepted 21 July 2007
Available online 22 August 2007

Abstract

The single-phase 6H $BaRuO_3$ with the hexagonal $BaTiO_3$ structure was synthesized at 5 GPa and 1000 °C. Rietveld refinement of the powder X-ray data for the 6H phase resulted in the lattice parameters to be $a = 5.7127(1)$ Å and $c = 14.0499(2)$ Å; the average Ru–O distance and direct Ru–Ru distance in the Ru_2O_9 dioctahedron being 1.992(6) and 2.5658(14) Å, respectively. The electrical resistivity of the 6H $BaRuO_3$ follows a relationship of ρ versus $T^{3/2}$ below 60.0 K, a signature deviation from the Fermi-liquid behavior. Both magnetic susceptibility and specific heat data indicate that the 6H $BaRuO_3$ is an exchange-enhanced Pauli paramagnet due to the electron correlation effect with large Wilson ratio R_W and Stoner enhancement factor. The comprehensive evolution of transport and magnetic properties from 9R across 4H to 6H $BaRuO_3$ was discussed.

Keywords: High-pressure synthesis; Ruthenate polymorphs; 6H-perovskite; Electrical conductivity; Specific heat; Rietveld analysis; Enhanced Pauli paramagnet; Electron correlation effects

1. Introduction

The oxide ruthenates have received growing attention for their unique physical properties. For example, in the Ruddlesden–Popper series $Sr_{n+1}Ru_nO_{3n+1}$ ($n = 1$, 2, 3, and infinity), Sr_2RuO_4 is a superconductor of unconventional *p*-wave paring mechanism [1], while $SrRuO_3$ is a ferromagnetic metal, with the Curie temperature of about 164 K [2]. $Sr_3Ru_2O_7$ is a metamagnetic metal, and its magnetic behavior has not been fully understood so far [3,4]. Most of ruthenates, e.g. $CaRuO_3$ [5], $La_4Ru_6O_{19}$ [6], $Sr_3Ru_2O_7$ [7], and $Ba_2Ru_7O_{18}$ [8], demonstrated a non-Fermi-liquid behavior accompanied with unconventional magnetic properties, which were partly ascribed to the orbital ordering effects due to the novel electronic structure of Ru oxides [9].

The alkaline-earth ruthenate $ARuO_3$ (where A is the alkaline-earth element Ca, Sr, and Ba) is an important system of oxide ruthenates [10]. However, the crystal structure and physical property of $ARuO_3$ strongly depend on size of *A*-site cations. For example, $SrRuO_3$ and $CaRuO_3$ adopt the orthorhombic perovskite structure with the space group *Pnma*. The former is a ferromagnetic metal [2], while the latter is a paramagnetic metal [11]. On the other hand, although being chemically related to $SrRuO_3$ and $CaRuO_3$, the structure of $BaRuO_3$ is quite different from that of them. The large *A*-site ion gives rise to a tolerant factor $t \sim 1.054$ ($t = (A–O)/2^{1/2}(B–O)$, where A–O and B–O is the atomic distance in the ABO_3 form) in the assumed cubic $BaRuO_3$ as calculated from the ion radii in Shannon Table [12]. This makes it difficult to synthesize $BaRuO_3$ with cubic perovskite structure since the usual *t* factor to accommodate a cubic perovskite is less than or equal to 1. Rather $BaRuO_3$ crystallizes into the rhombohedral (space group: *R*-3*m*) or hexagonal (space group: $P6_3/mmc$) structure at ambient or lower pressure [13,14]. In $BaRuO_3$, Ba and O ions can form BaO_3 layer by close stacking mode. The Ru cation fills the interspace of O anions and forms RuO_6 octahedrons. There are two modes of stacking between the two adjacent BaO_3 layers: hexagonal close stacking (*h*) and cubic close stacking (*c*), which corresponds to the face-shared and corner-shared connections between the two neighboring RuO_6 octahedrons,

*Corresponding author. Fax: +86 10 82649531.
E-mail address: jin@aphy.iphy.ac.cn (C.Q. Jin).

0022-4596/$ - see front matter © 2007 Elsevier Inc. All rights reserved.
doi:10.1016/j.jssc.2007.07.031

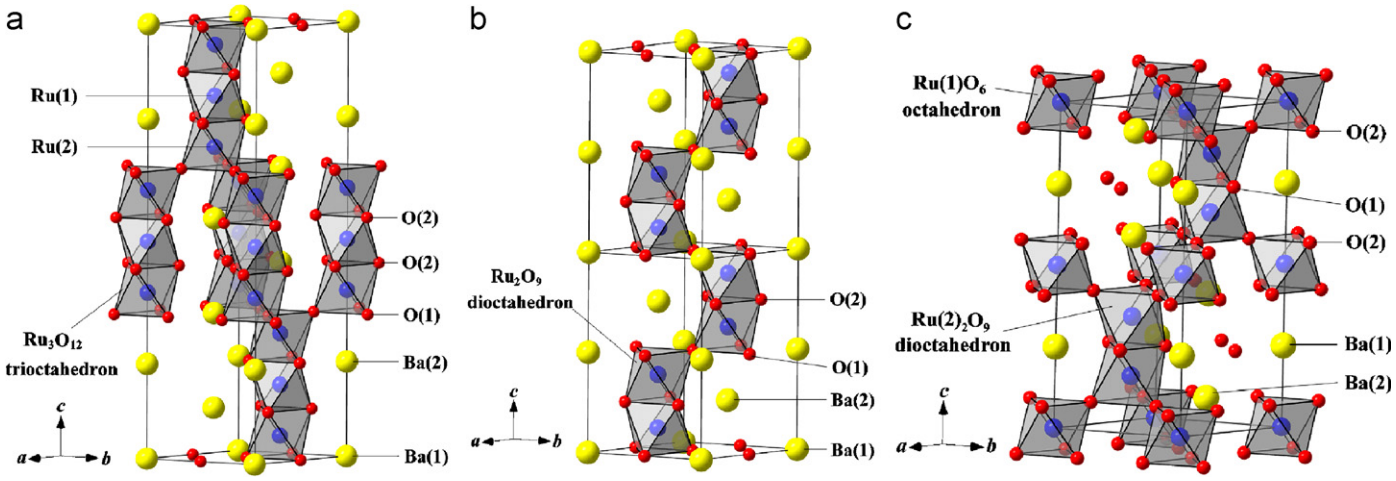

Fig. 1. The schematic views of the three crystallographic forms of $BaRuO_3$. (a) 9R form, (b) 4H form and (c) 6H form. The RuO_6 octahedrons are represented by geometrical coordination (Ru at the center, O at corners). The unit cells are outlined.

respectively. There are so far three types of hexagonal perovskite-type $BaRuO_3$ reported, namely 9R, 4H, and 6H, corresponding to the different stacking sequence of BaO_3 layers in a unite cell, where the number is the amount of BaO_3 layers in a unit cell, and the R and H denote the rhombohedral and hexagonal structures, respectively.

The 9R $BaRuO_3$ can be obtained through the conventional solid-state chemical reaction [13]. Three RuO_6 octahedrons stack together with face-shared connections to form one Ru_3O_{12} trioctahedron. These trioctahedrons connect each other through the O anions in the corner, so the stacking sequence is *hhchhchhc*. The 4H $BaRuO_3$ was initially synthesized as a high-pressure phase [14]. But, recently, it was reported by Sleight group [15] and Cava group [16] that the 4H $BaRuO_3$ can also be prepared at ambient pressure using soft chemistry method. The stacking sequence of BaO_3 layers could be denoted as *hchc*. The electrical and magnetic properties of the 4H $BaRuO_3$ are quite different from those of the 9R $BaRuO_3$, implying that the different connections of the neighboring RuO_6 octahedrons have significant effects on the electronic and spin orientation states. The temperature dependence of resistivity of the 9R $BaRuO_3$ shows a transition from metallic to insulator-like behavior at about 110 K [16,17] that is believed due to the pseudogap open. The 9R $BaRuO_3$ is of short-range antiferromagnetic order at high temperature, with the Néel point about 440 K, due to the antiferromagnnetic arrangement between the adjacent electronic spin in the Ru_3O_{12} trioctahedrons [17,18]. However, the 4H $BaRuO_3$ is a paramagnetic metal [16]. While the pressure exceeds 3.0 GPa at 1000 °C, the 6H $BaRuO_3$, with the hexagonal $BaTiO_3$ structure [19], begins to come forth as a mixed phase with the 9R or 4H forms [14]. In the 6H $BaRuO_3$, the Ru_2O_9 dioctahedron and RuO_6 octahedron arrange alternately and connect each other through the O anions. The stacking sequence is *hcchcc*. The schematic views of the three crystallographic forms of $BaRuO_3$ are shown in Fig. 1. However, characterizing the physical or structural properties of the pure 6H $BaRuO_3$ and thus to map a comprehensive correlations between the RuO_6 polyhedron connections with their physics have not been available so far due to the difficulty to prepare single-phase 6H $BaRuO_3$.

In this paper, we report that a pure 6H $BaRuO_3$ compound was successfully obtained by using the high-pressure and high-temperature synthesis method. For the first time the structural detail based on Rietveld refinement, together with the systematic characterization of electrical and magnetic properties of the 6H $BaRuO_3$ was obtained.

2. Experimental

2.1. Synthesis

The 9R $BaRuO_3$ was synthesized by using the method of conventional solid-state chemical reaction. The starting materials were barium carbonate (99.9% purity) and ruthenium metal (99.9% purity). Stoichiometric quantities of materials were mixed and ground about 30 min in an agate mortar. Then the powder was sintered for about 12 h at 1000 °C in air. The calcined powder was reground, pressed into a pellet at the pressure of 10 MPa, and sintered at 1100 °C for about 48 h in air with one intermediate regrinding. The product was black polycrystalline.

A conventional cubic-anvil type high-pressure facility was used to perform the high-pressure and high-temperature experiments. The 9R $BaRuO_3$ material was pressed into pellets of 5.0 mm diameter, and then wrapped with gold foil to avoid contamination. The pellets were put into an h-BN sleeve which was in turn inserted into a graphite tube heater. Pyrophyllite was used as the pressure-transmitting medium. The treating process was carried out at 2.5–5.0 GPa and 1000 °C for about 30 min, followed by a quench from high temperature before releasing pressure with the rate about 0.6 GPa/min. The products

were the 6H form at 5.0 GPa and the 4H form at 2.5 GPa, which were both black and hard bulk.

2.2. X-ray diffraction analysis

The structures of our samples were checked by the powder X-ray diffraction (XRD) with Cu-K_α radiation at room temperature, using a Rigaku diffractometer (MXP-AHP18). The experimental data of the 6H $BaRuO_3$ were collected in 2θ-steps of 0.02° and 3 s counting time in the range $10° \leqslant 2\theta \leqslant 120°$ and analyzed with Rietveld method by using the FullProf program [20].

2.3. Electrical resistivity measurements

The measurements of temperature dependences of electrical resistivity in the range 3–300 K were performed by using the standard four-probe method with Ag paste contacts on an Oxford Maglab measuring system.

2.4. Magnetic susceptibility measurements

The relationships of magnetic susceptibility versus temperature were obtained using a SQUID magnetometer (Quantum Design, MPMS-5S) in the temperature range 5–300 K. Data were collected under both zero-field-cooled (ZFC) and field-cooled (FC) conditions in a 1 T applied field. For the 6H $BaRuO_3$, the magnetic field dependence of magnetization was measured at 5 K with $0\,T \leqslant H \leqslant 5\,T$.

2.5. Specific heat measurements

The heat-capacity measurements were carried out using a heat pulse relaxation technique with a commercial heat capacity measuring system (Quantum Design, PPMS equipment) in the range 2–50 K. The samples were mounted on a thin alumina plate with grease for better thermal contact.

3. Results and discussion

3.1. Crystal structure

Fig. 2 shows the observed and fitted XRD patterns of the 6H $BaRuO_3$, and the inset shows the details in the range 80–120°. The data are fitted with the $P6_3/mmc$ space group and analyzed with the Rietveld method. The obtained R_p, R_{wp}, and R_{exp} factors are 6.12%, 8.47%, and 7.54%, respectively, indicating the good consistence of the refined results. The lattice parameters are refined to be $a = 5.7127(1)$ Å and $c = 14.0499(2)$ Å, respectively. Table 1 lists the positional parameters, and Table 2 lists the main interatomic distances and bond angles. The details of the $Ru(2)_2O_9$ dioctahedron and single $Ru(1)O_6$ octahedron are shown in Fig. 3. Parts of bond distances and bond angles are also marked in this view. The Ru(2)–Ru(2) distance is 2.5658(14) Å for the two Ru cations connected directly in the Ru_2O_9 dioctahedron. The Ru(1)–O–Ru(2) distance is 3.9811(6) Å for the two Ru cations connected through the O anion in the corner. The O(2)-Ru(1)-O(2) angles are nearly equal to 90° or 180°, indicating that the $Ru(1)O_6$ octahedron is almost ideal without bond bending. On the other hand the O(1)–Ru(2)–O(1), O(2)–Ru(2)–O(2), and

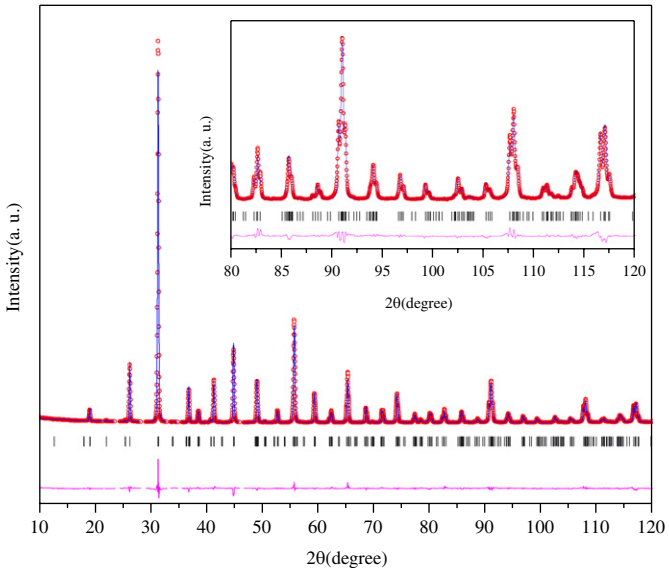

Fig. 2. The experimental (open circle) and fitted (solid line) X-ray diffraction patterns for the 6H $BaRuO_3$. The difference plot between observed and calculated pattern is shown at the bottom. The positions of the Bragg reflections are shown by the vertical lines. The inset shows the detail of patterns in the range 80–120°.

Table 1
Atomic coordinates of the 6H $BaRuO_3$ obtained through Rietveld refinement of powder X-ray diffraction

Atom	Site	x	y	z	B (Å^2)
Ba(1)	2b	0	0	1/4	0.35(3)
Ba(2)	4f	1/3	2/3	0.08960(6)	0.22(2)
Ru(1)	2a	0	0	0	0.62(4)
Ru(2)	4f	1/3	2/3	0.65869(6)	0.40(3)
O(1)	6h	0.5168(7)	0.0337(14)	1/4	1.7(2)
O(2)	12k	0.8362(8)	0.6724(16)	0.0782(3)	0.4(1)

Table 2
Selected bond distances (Å) and angles (deg.) of the 6H $BaRuO_3$

Bond	Distance (Å)	Bond	Angle (deg.)
Ba(1)–O(1) × 6	2.861(3)	O(1)–Ru(2)–O(1) × 3	81.8
Ba(1)–O(2) × 6	2.907(6)	O(2)–Ru(2)–O(2) × 3	91.8(2)
Ba(2)–O(2) × 6	2.861(3)	O(1)–Ru(2)–O(2) × 6	93.0(1)
Ba(2)–O(2) × 3	2.894(6)	O(1)–Ru(2)–O(2) × 3	173.1(1)
Ba(2)–O(1) × 3	2.894(4)	O(2)–Ru(1)–O(2) × 6	88.4(2)
Ru(1)–O(2) × 6	1.958(5)	O(2)–Ru(1)–O(2) × 6	91.6(2)
Ru(2)–O(1) × 3	1.960(4)	O(2)–Ru(1)–O(2) × 3	180.0(3)
Ru(2)–O(2) × 3	2.023(7)	Ru(2)–O(1)–Ru(2)	81.7
Ru(1)–Ru(2)	3.9811(6)	Ru(1)–O(2)–Ru(2)	179.9(3)
Ru(2)–Ru(2)	2.5658(14)		

O(1)–Ru(2)–O(2) angles deviate from 90° or 180°. So it can be concluded that the distortion of the $Ru(2)_2O_9$ dioctahedron is larger than that of the $Ru(1)O_6$ octahedron.

The lattice parameters of the 9R, 4H, and 6H $BaRuO_3$ are summarized in Table 3, based on the data in Ref. [15,21] and this work, respectively. The ratio of c to na and the volume per one chemical formula unit (V/n) are obtained, where n is the amount of AO_3 layers and V is the volume of one unit cell. The shrinkage of V/n for the 6H $BaRuO_3$ is about 3.6% and 2.0%, comparing with the 9R and 4H forms, respectively. The average Ru–O distance d_{Ru-O} and direct Ru–Ru distance d_{Ru-Ru} in the polyhedron for the three forms are also provided. The average Ru–O distance is decreasing with decreasing V/n. This is consistent with the fact that the unit cell is more compact from 9R across 4H to 6H with gradually increasing synthesis pressure, leading to the shrink of Ru–O atomic distance. But the compensating distortion of the Ru_2O_9 cluster increases the Ru–Ru distance in the 6H $BaRuO_3$. For the three forms of $BaRuO_3$, the direct Ru–Ru distances in the polyhedron are shorter than the separation in ruthenium metal (2.65 Å), suggesting that the 9R, 4H or 6H polymorphs could be basically metal like. From the large bulk modulus of 320.8 GPa for ruthenium metal [22], it can be deduced that there is strong repulsion between the Ru cations in $BaRuO_3$.

In order to compare the structure of the three forms, the hexagonal unit cell is normalized to a "cubic" form by using the following equations:

$$a_N = \sqrt{2}a/2, \quad (1)$$

$$c_N = \sqrt{3}c/n \quad (2)$$

to calculate the normalized lattice parameters for an assumed pseudo cubic perovskite form. The Eqs. (1) and (2) indicate that the hexagonal structure contains a sequence of n close-packed layers, with each layer consisting of the same ions of the (1 1 1) plane in the cubic structure [19]. Fig. 4 shows the roughly linear relationship of c_N and a_N versus V/n, and the inset shows the ratio of c_N to a_N. The c_N is larger than a_N for all the three forms of $BaRuO_3$, due to the repulsion between the neighboring Ru cations in the polyhedron, which is different from the equality between a_N and c_N for the 6H $BaTiO_3$ [19]. The c_N and a_N are both decreasing with decreasing V/n, but a_N decreases more slowly, so the difference between c_N and a_N is becoming small from 9R across 4H to 6H phase, as shown in the inset of Fig. 4. So $BaRuO_3$ will eventually become pseudo-cubic or cubic at sufficient high synthesis pressure.

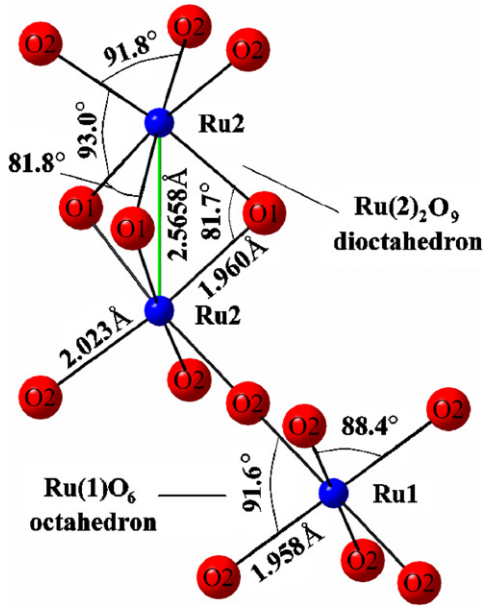

Fig. 3. Details of the $Ru(2)_2O_9$ dioctahedron and single $Ru(1)O_6$ octahedron. Parts of bond distances and bond angles are also shown.

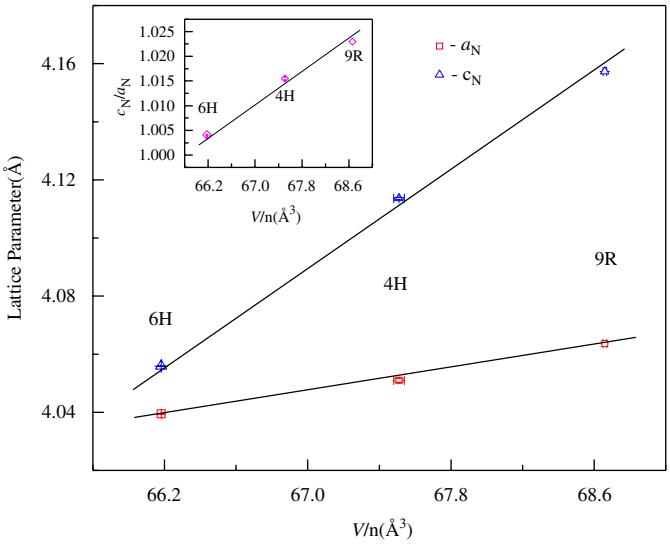

Fig. 4. The relationship of normalized lattice parameter a_N and c_N versus the volume of one chemical formula unit (V/n) for the 9R, 4H, and 6H $BaRuO_3$. The inset shows the ratio of c_N to a_N with V/n.

Table 3
The structural parameters of the 9R, 4H, and 6H $BaRuO_3$

Phase (space group)	a (Å)	c (Å)	$c/(na)$	V/n (Å^3)	d_{Ru-O} (Å)	d_{Ru-Ru} (Å)
9R(R-3m)	5.747	21.602	0.4177	68.66(1)	2.002	2.543
4H($P6_3/mmc$)	5.729(1)	9.500(1)	0.4146(1)	67.51(3)	1.996(2)	2.537(1)
6H($P6_3/mmc$)	5.7127(1)	14.0499(2)	0.40990(1)	66.181(2)	1.992(5)	2.5658(14)

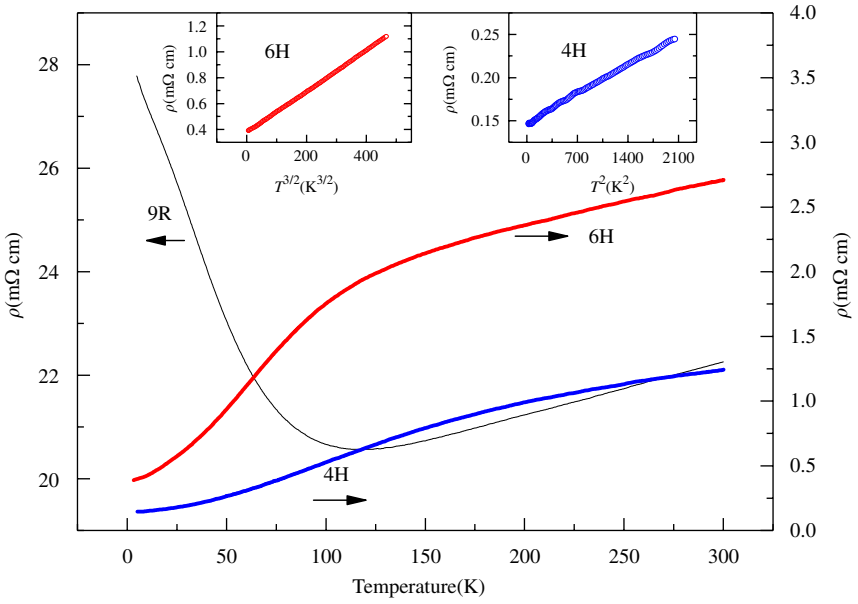

Fig. 5. Temperature dependences of electrical resistivity of the 9R, 4H, and 6H $BaRuO_3$. The inset shows the linear relationship of electrical resistivity versus $T^{3/2}$ of the 6H form and that versus T^2 of the 4H form.

3.2. Electrical properties

The temperature dependences of electrical resistivity in the range 3–300 K of the 9R, 4H, and 6H $BaRuO_3$ are shown in Fig. 5. It is clear that the 9R $BaRuO_3$ is a metal at high temperature roughly following a linear relation of ρ versus T and becomes insulator like at lower temperature, with the metal–insulator transition (MIT) temperature T_{MI} about 118 K. This metal–insulator transition was believed to result from a pseudogap open at low temperature [17]. The 4H and 6H $BaRuO_3$ maintain the metallic behavior down to the lowest temperature in our experiments. However, the resistivities for the 4H and 6H forms do not show the linear dependence on temperature above 150 K, as predicated by phonon scattering mechanism based on extended band theory, which is different from that of the 9R $BaRuO_3$. The electrical resistivity of the 4H $BaRuO_3$ at low temperature follows approximately the equation $\rho = \rho_0 + AT^2$, indicating that it still is a Fermi-liquid metal, being consistent with the result in Ref. [16]. The inset at top right corner of Fig. 5 shows the linear relationship of ρ versus T^2. The residual resistivity ratio ($RRR = \rho_{300K}/\rho_{T\to 0}$) for the 4H $BaRuO_3$ is approximately equal to 8. On the other hand the 6H $BaRuO_3$ cannot be ready fitted to the relationship of ρ versus T^2. We found that the resistivity of the 6H $BaRuO_3$ could alternatively be better described by the relationship of ρ versus $T^{3/2}$, as shown in the inset of Fig. 5. The fitted results of electrical properties of the 4H and 6H forms are summarized in Table 4. The residual resistivity ratio of the 6H $BaRuO_3$ is equal to about 7, which is less than that of the 4H form. From the results of residual resistivity ratio, the metallicity of the 4H $BaRuO_3$ is better than that of the 6H form. This can be ascribed to (1) the 4H phase has a higher proportion of direct Ru–Ru interaction than that in the 6H phase; (2) the Ru–Ru distance in the 4H form is shorter, as discussed in the structural analysis, which makes the electrons more itinerant. The deviation from the equation $\rho = \rho_0 + AT^2$ for the electrical resistivity at low temperature indicates that there exists non-Fermi-liquid behavior in the 6H $BaRuO_3$. This is quite different from the 4H form, indicating the enhanced electron correlations in the 6H $BaRuO_3$ due to the increased portion of corner-shared RuO_6 octahedron. The non-Fermi-liquid behavior widely exists in the ruthenates [5–8], where the corner-shared RuO_6 octahedron is predominated leading to spin orbital coupling and enhanced electron correlations [9].

Table 4
Fitted results of ρ–T curves in the form ($\rho = \rho_0 + AT^n$) and residual resistivity ratio RRR ($\rho_{300\,K}/\rho_{T\to 0}$) for the 4H and 6H $BaRuO_3$

	4H	6H
Range (K)	5–45	3–60
n	2	3/2
ρ_0 (mΩ cm)	0.1532(3)	0.3742(4)
A (μΩ cm/K^n)	$5.58(5)\times 10^{-2}$	1.590(1)
RRR	8.11(2)	7.237(8)

Unlike the quasi one-dimensional chain-type structure for the 9R $BaRuO_3$ being composed of Ru_3O_{12} trioctahedron and the 4H $BaRuO_3$ being composed of Ru_2O_9 dioctahedron, the arrangement of Ru cations in the 6H form is more close to three-dimension in that it has a single-corner-shared RuO_6 octahedron between two Ru_2O_9 dioctahedrons, indicating the higher portion of corner-shared RuO_6 octahedron than those of the former two phases. So the structure of the 6H $BaRuO_3$ is intermediate between the 4H and cubic phase. The superexchange

interaction between Ru(1) and Ru(2) cations is thus more important in the 6H $BaRuO_3$. This Ru–O–Ru superexchange interaction usually cause unconventional electronic state and electrical transport property [5–8] that deviates from normal Fermi-liquid metal due to the improved orbital coupling and strong electron correlation effects [9]. For example, the corner-shared $CaRuO_3$ ruthenate perovskite is a non-Fermi-liquid metal [5]. The non-Fermi-liquid behavior was also found in the corner-shared $SrRuO_3$ perovskite by measuring infrared conductivity [23]. Even in the 4H $BaRuO_3$, there is also signature about the non-Fermi-liquid behavior, as obtained from the failure of Kohler's rule in the magnetoresistance scaling [24]. On the other hand it is well known that the physical properties of ruthenates are very sensitive to disorder from vacancy or impurity [25]. The influence of disorder from oxygen vacancy might also exist in our 6H $BaRuO_3$ sample. We indeed post annealed the as prepared sample in O_2 or Ar atmosphere in order to eliminate the possible disorder caused by oxygen vacancy or interstitial oxygen. However, there is little effect of the post anneal on overall transport properties. Therefore we inferred that the non-Fermi-liquid behavior shown for the present 6H $BaRuO_3$ is intrinsic, most likely due to the increased Ru–O–Ru interaction caused by the corner-shared octahedron connection.

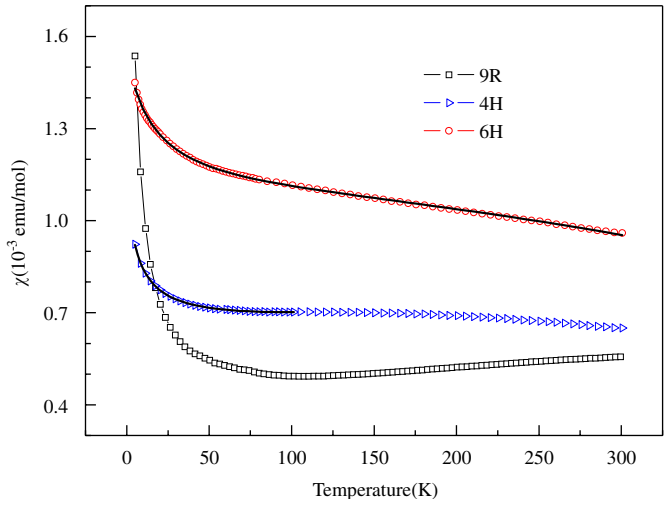

Fig. 6. Temperature dependences of magnetic susceptibility of the 9R, 4H, and 6H $BaRuO_3$. The solid lines are the fit to the data of the 4H and 6H forms using the Eq. (3).

3.3. Magnetic properties and specific heat

Fig. 6 shows the temperature dependence of magnetic susceptibility in the range 5–300 K of the 9R, 4H, and 6H $BaRuO_3$. Since there is no obvious deviation between ZFC and FC curves for the three forms, Fig. 6 only shows the ZFC mode. The χ–T curves of the 9R and 4H $BaRuO_3$ are similar with the previous results in Refs. [16–18]. The magnetic susceptibility shows weak temperature dependence in the range 100–300 K and the slightly enhanced temperature dependence at lower temperature. According to the χ–T curve, the 9R $BaRuO_3$ is short-range antiferromagnetic at high temperature, and is paramagnetism like at low temperature, being similar with the results in Refs. [17,18]. The 4H and 6H forms are both paramagnetic. The value of magnetic susceptibility is 6.5×10^{-4} and 9.6×10^{-4} emu/mol at 300 K for the 4H and 6H forms, respectively. Fig. 7(a) shows the magnetic

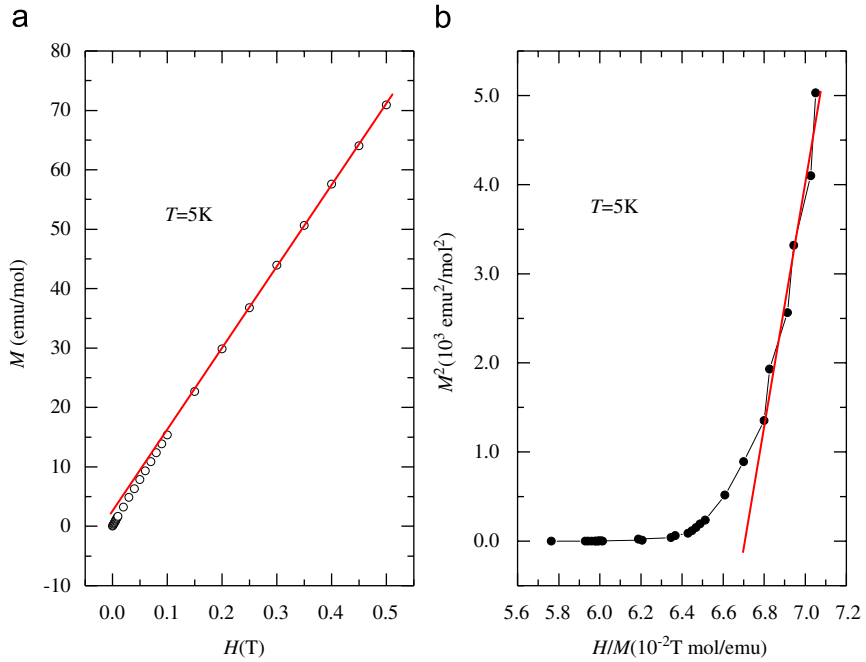

Fig. 7. (a) The relationship of magnetization versus magnetic field at 5 K for the 6H $BaRuO_3$; (b) The relationship of M^2 versus H/M converted from (a).

field dependence of magnetization at 5 K for the 6H $BaRuO_3$, which indicates no long-range ferromagnetic order in this sample. The concave downward curvature at low fields in the M–H curve indicates the exchange-enhanced paramagnetism of the 6H form [26]. The Arrott plot is shown in Fig. 7(b), as converted from (a). The negative intercept on the M^2 axis, as obtained from the linear extrapolation of the high-field portion of M^2–(H/M) curve to $H = 0$, indicates that no spontaneous magnetization exits at 5 K for the 6H $BaRuO_3$ [27]. Both the 4H and 6H $BaRuO_3$ are electron correlation enhanced Pauli paramagnetic due to the increased portion of corner-shared RuO_6 octahedron in the unit cell, leading to less temperature sensitive but much higher magnetic susceptibility. Taking into account the electron correlation, the paramagnetic susceptibility χ of a metal can be revised into the expression [26]:

$$\chi = \chi_{CW}(T) + \chi_{EP}(T) = \frac{C}{T-\theta} + \chi_0(1 - AT^2), \quad (3)$$

where χ_{CW} and χ_{EP} are the Curie–Weiss (CW) and exchange-enhanced Pauli (EP) contributions to magnetic susceptibility, respectively. The fitted curves of the 4H and 6H forms are denoted with the solid lines in Fig. 6, and the fitted results to magnetic properties are summarized in Table 5. For the 6H $BaRuO_3$, in the temperature range of 5–300 K, the Curie constant C is $8.4(2) \times 10^{-3}$ emu K/mol; the paramagnetic Curie temperature θ is $-17.5(5)$ K; the temperature independent magnetic susceptibility χ_0 is $1.056(2) \times 10^{-3}$ emu/mol; and A is $1.35(2) \times 10^{-6}$ K^{-2}. The effect magnetic moment per Ru atom (μ_{eff}) is 0.259(3) μ_B, as obtained from Curie constant C through the formula $\mu_{eff} = 2.83\sqrt{C}$, which is smaller than the theoretic value of about 2.83 μ_B calculated in the spin only model for the two unpaired 4d electrons in the Ru^{4+} cations. This indicates that there is spin orbital coupling effect for the compound. The fitted μ_{eff} of the 4H $BaRuO_3$ is smaller than that of the 6H form, due to the absence of single RuO_6 octahedron. For the 4H and 6H forms, the small value of μ_{eff} indicates that the Ru cation loses partly local moment, which is contributed to the improved itinerancy resulting from the direct interaction between adjacent Ru cations in the Ru_2O_9 dioctahedrons and the strong spin–orbit coupling for Ru cations. The negative sign of θ indicates that the interaction between the spins on the nearest-neighbour sites should be antiferromagnetic in the Ru_2O_9 dioctahedron, as suggested for Ru-site substitution compounds of $BaRuO_3$ [28]. For the 4H and 6H $BaRuO_3$, χ_0 is orders of magnitude higher than that of free electron system, which confirms that they are the electron exchange-enhanced Pauli paramagnet due to the 4d transition metal nature.

Table 5
Fitted results of χ–T curves of the 4H and 6H $BaRuO_3$ in the form of $\chi = \chi_{CW}(T) + \chi_{EP}(T) = \frac{C}{T-\theta} + \chi_0(1 - AT^2)$

	4H	6H
C (10^{-3} emu K/mol)	3.07(7)	8.4(2)
μ_{eff} (μ_B)	0.157(2)	0.259(3)
θ (K)	−6.7(2)	−17.5(5)
χ_0 (10^{-4} emu/mol)	6.58(1)	10.56(2)
A (10^{-6} K^{-2})	−2.3(2)	1.35(2)

In order to investigate more about the physical property of $BaRuO_3$, we measured the low-temperature specific heat, with the C–T curves of the three polymorphs in the range 2–50 K being shown in Fig. 8. The curves do not show the λ-type anomalies in the experimental temperature range, indicating that there is not long-range magnetic order or phase transition, being consistent with the results of magnetic susceptibility. For the 9R and 6H $BaRuO_3$, the specific heat below 10 K can be fitted to the following equation:

$$C/T = \gamma + \beta T^2, \quad (4)$$

where the first term is the electronic contribution, and the second term is the phonon contribution according to the Debye approximation. For the 4H $BaRuO_3$, the specific heat below 10 K can be fitted to the following equation:

$$C/T = \gamma + \beta T^2 + \delta T^4, \quad (5)$$

where the first and second terms are same with those in Eq. (4), and the third term is the deviation from the linear dispersion of the acoustic modes in extended temperature range. The relationships of C/T versus T^2 are shown in the inset of Fig. 8. The fitted results to the specific heat are summarized in Table 6. For the 6H $BaRuO_3$, the β is 0.206(2) mJ/(mol K^4), so the Debye temperature Θ_D is 361(1) K, as obtained from the formula $\Theta_D = (1.944 \times 10^6 p/\beta)^{1/3}$, where p is the number of atoms per chemical formula unit, and has the value $p = 5$ for $BaRuO_3$. The Sommerfeld constant γ is 27.62(8) mJ/(mol K^2). So the Wilson ratio R_W ($R_W = 1/3(\pi k_B/\mu_B)^2(\chi_0/\gamma)$) is equal to 2.50(1), which is much larger than the

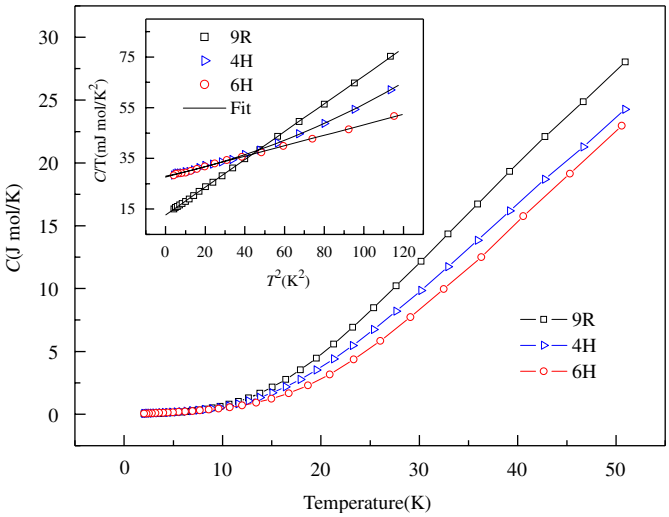

Fig. 8. Low-temperature specific heat of the 9R, 4H, and 6H $BaRuO_3$. The inset shows the relationships of C/T versus T^2.

Table 6
Fitted results of C–T curves of the 9R and 6H $BaRuO_3$ in the form of $C/T = \gamma + \beta T^2$, and of the 4H $BaRuO_3$ in the form of $C/T = \gamma + \beta T^2 + \delta T^4$

	9R	4H	6H
γ (mJ/mol K^2)	12.64(7)	27.96(9)	27.62(8)
β (mJ/mol K^4)	0.549(1)	0.165(5)	0.206(2)
δ (mJ/mol K^6)	–	$1.19(5)\times10^{-3}$	–
Θ_D (K)	260.6(2)	389(4)	361(1)
R_W	–	1.718(8)	2.50(1)
S	–	5.82	9.35
$IN(E_F)$	–	0.83	0.89

value of 1 for the free electron system [29], indicating the strong electron–electron correlation in the 6H $BaRuO_3$. The γ of the 9R $BaRuO_3$ is closely equal to the result of single-crystal sample in Ref. [10]. For the 4H $BaRuO_3$, the γ is approximately equal to that of the 6H form, and the large R_W indicates the strong electron–electron correlation, like that of the 6H form. Assuming the density of state at Fermi energy level $N(E_F)$ of the 6H $BaRuO_3$ is comparable to that of the 4H form because of the similar crystal structure feature, we chosen the $N(E_F)$ of 3.5 state/(eVf.u.) for the 4H phase [30] as the theoretic value of the 6H $BaRuO_3$, since no energy band structure calculation has been performed for the 6H $BaRuO_3$ so far. Therefore the theoretic γ^{th} of the three polymorphs is equal to 8.2 mJ/(mol K^2), as calculated from $N(E_F)$ through the formula $\gamma^{th} = \pi^2 k_B^2 N(E_F)/3$. For the 4H and 6H forms, the enhancement of the effective mass $m^*/m_0 = \gamma/\gamma^{th} = 3.37$ was obtained, so the contribution of Landau diamagnetic susceptibility to χ_0 is small, as valid to most strong-correlation materials. Therefore the Pauli paramagnetic susceptibility χ_p is approximately equal to χ_0. According to this $N(E_F)$, the theoretic Pauli paramagnetic susceptibility χ_p^{th} is 1.13×10^{-4} emu/mol, as calculated from $N(E_F)$ through the formula $\chi_p^{th} = \mu_B^2 N(E_F)$, which is less than the experimental value. The specific data confirms that electron correlation effect is significant in the $BaRuO_3$ polymorphs. The calculated Stoner enhancement factor S ($S = \chi_p/\chi_p^{th} = [1\text{-}IN(E_F)]^{-1}$) is equal to 5.82 and 9.35 for the 4H and 6H forms, respectively, where I is the exchange integral that reflects the exchange splitting of energy band. So $IN(E_F)$ is equal to 0.83 and 0.89 for the 4H and 6H forms, respectively. The large Stoner enhancement gives rise to the large Wilson ratio. Therefore the results of magnetic susceptibility and specific heat clearly indicate there is strong electron–electron correlation in the 4H and 6H $BaRuO_3$.

4. Summary

The single-phase 6H $BaRuO_3$ was synthesized using the high-pressure technique, and the XRD pattern, electrical resistivity, magnetic susceptibility, and specific heat were obtained. Rietveld refinement based on X-ray diffraction indicated that it crystallizes into the hexagonal $BaTiO_3$ structure. The measurements of electrical and magnetic properties showed that the 6H $BaRuO_3$ is an abnormal paramagnetic metal deviation from the Fermi liquid behavior. The large Wilson ratio R_W and Stoner enhancement indicated a strong electron–electron correlation in the compound.

Acknowledgments

This work was supported by NSF and Ministry of Science and Technology of China through the research projects (2005CB724402, 50332020, 10674160). We are grateful to J.S. Zhou for the helpful discussions.

References

[1] Y. Maeno, H. Hashimoto, K. Yoshida, S. Nishizaki, T. Fujita, J.G. Bednorz, F. Lichtenberg, Nature 372 (1994) 532–534.
[2] A. Callaghan, C.W. Moeller, R. Ward, Inorg. Chem. 5 (1966) 1572–1576.
[3] R.J. Cava, H.W. Zandbergen, J.J. Krajewski, W.F. Peck, B. Batlogg, S. Carter, R.M. Fleming, O. Zhou, L.W. Rupp, J. Solid State Chem. 116 (1995) 141–145.
[4] G. Cao, S. McCall, J.E. Crow, Phys. Rev. B 55 (1997) R672–R675.
[5] L. Klein, L. Antognazza, T.H. Geballe, M.R. Beasley, A. Kapitulnik, Phys. Rev. B 60 (1999) 1448–1451.
[6] P. Khalifah, K.D. Nelson, R. Jin, Z.Q. Mao, Y. Liu, Q. Huang, X.P.A. Gao, A.P. Ramirez, R.J. Cava, Nature 411 (2001) 669–671.
[7] S.A. Grigera, R.S. Perry, A.J. Shofield, M. Chiao, S.R. Julian, G.G. Lonzarich, S.L. Ikeda, Y. Maeno, A.J. Millis, A.P. Mackenzle, Science 294 (2001) 329–332.
[8] T. Ogawa, H. Sato, J. Alloys Compd. 383 (2004) 313–318.
[9] Z. Fang, K. Terakura, N. Nagaosa, New J. Phys. 7 (2005) 66–81.
[10] M. Shepard, S. McCall, G. Cao, J.E. Crow, J. Appl. Phys. 81 (1997) 4978–4980.
[11] J.M. Longo, P.M. Raccah, J.B. Goodenough, J. Appl. Phys. 39 (1968) 1327–1328.
[12] R.D. Shannon, Acta Cryst. A 32 (1976) 751–767.
[13] P.C. Donohue, L. Katz, R. Ward, Inorg. Chem. 4 (1964) 306–310.
[14] J.M. Longo, J.A. Kafalas, Mater. Res. Bull. 3 (1968) 687–692.
[15] S.-T. Hong, A.W. Sleight, J. Solid State Chem. 128 (1997) 251–255.
[16] J.T. Rijssenbeek, R. Jin, Y. Zadorozhny, Y. Liu, B. Batlogg, R.J. Cava, Phys. Rev. B 59 (1999) 4561–4564.
[17] Y.S. Lee, J.S. Lee, K.W. Kim, T.W. Noh, J. Yu, E.J. Choi, G. Cao, J.E. Crow, Europhys. Lett. 55 (2001) 280–286.
[18] M. Drillon, L. Padel, J.-C. Bernier, J. Chem. Soc. Faraday Trans. II 75 (1979) 1193–1198.
[19] R.D. Burbank, H.T. Evans, Acta Cryst. 1 (1948) 330–336.
[20] R.A. Young, The Rietveld Method, IUCr/OUP, Oxford, 1995.
[21] M.V.R. Rao, V.G. Sathe, D. Sornadurai, B. Panigrahi, T. Shripathi, J. Phys. Chem. Solids 62 (2001) 797–806.
[22] K. Gschneidner Jr., Solid State Phys. 16 (1964) 275–426.
[23] P. Kostic, Y. Okada, N.C. Collins, Z. Schlesinger, J.W. Reiner, L. Klein, A. Kapitulnik, T.H. Geballe, M.R. Beasley, Phys. Rev. Lett. 81 (1998) 2498–2501.
[24] S. Levy, Y. Kats, M.K. Lee, C.B. Eom, L. Klein, Physica B 312–313 (2002) 795–796.
[25] L. Capogna, A.P. Mackenzie, R.S. Perry, S.A. Grigera, L.M. Galvin, P. Raychaudhuri, A.J. Schofield, C.S. Alexander, G. Cao, S.R. Julian, Y. Maeno, Phys. Rev. Lett. 88 (2002) 076602.
[26] S.N. Kaul, A. Semwal, H.-E. Schaefer, Phys. Rev. B 62 (2000) 13892–13895.
[27] A. Arrott, Phys. Rev. 108 (1957) 1394–1396.
[28] P. Lightfoot, P.D. Battle, J. Solid State Chem. 89 (1990) 174–183.
[29] K.G. Wilson, Rev. Mod. Phys. 47 (1975) 773–840.
[30] C. Felser, R.J. Cava, Phys. Rev. B 61 (2000) 10005–10009.